Journal of Nuclear Materials 389 (2009) 365–376

Contents lists available at ScienceDirect

Journal of Nuclear Materials

journal homepage: www.elsevier.com/locate/jnucmat

Effect of radiolytic hydrogen peroxide in tritiated water on the first passivity of titanium

G. Bellanger *

French Atomic Energy Commission, 10 Avenue de la Paix, F21260 Selongey, France

ARTICLE INFO

Article history:
Received 9 September 2008
Accepted 30 January 2009

ABSTRACT

Titanium is an interesting metallic material for nuclear applications. This is due to its passivity ensured by a compact and chemically stable oxide film that spontaneously covers the metal surface. This work aims at studying the electrochemical behavior of titanium in the presence of tritiated water at pH 4 and containing hydrogen peroxide generated by radiolytic reaction. Tritium in tritiated water always causes difficulties in corrosion. The corrosion potential can be either in the active or prepassive regions depending on the concentration of radiolytic oxidizing species and intermediate species formed on the surface in the active region. Therefore, the behavior of titanium was studied by cyclic voltammetry and electrochemical noise in situ to provide an indication of mechanisms, transient formation and instabilities of oxide in active region. In the prepassivity and passivity, according to the results of electrochemical impedance spectroscopy and coulometric curves, titanium is protected by a semiconductor layer essentially formed of TiO_2. Between the region of first and second passivity, oxide consists of a dielectric layer and a semiconductor layer. These two layers protect the titanium against corrosion.

1. Introduction

It is essential in highly concentrated tritiated water (^3H_2O) reprocessing facilities that there is no leakage from the processing circuit to the environment. As an example, industrial accidents were arisen in 1994–1998 with tritiated water released in a reinforced concrete shell for retention of doubtful effluents then in the sewage water treatment plant. To avoid corrosion, the equipment must be completely metallic. Since all the equipment in the facility is metallic, the selection of metals depends on their corrosion resistance. Engineers and designers use two types of materials as bearing in mechanical equipment, these being soft and hard bearing to protect from excessive wear in both sliding and rotating applications. Coatings are applied because it will be too costly to manufacture large parts from solid casting of the bearing material. But, it is difficult to find materials that exhibit large lifetime performance characteristics. Titanium is a material of choice for lifetime performance and anticorrosion reasons, and this why this metal has been selected. Tritium decays with the emission of 5.7 keV β^- particles and ν_e antineutrino. The energy is high enough to decompose water molecules locally along the path of the β^- particle with formation of free electrons and radiolytic hydrogen peroxide ($^3H_2O_2$) as reported by Bruggeman et al. [1], Burns and Moore [2], Linacre and Marsh [3] and Wright et al. [4].

Decay:

$$^3H_2O \rightarrow 2\,^3He + O^\bullet + 2\beta^- + \nu_e. \quad (1)$$

Radiolyse:

$$2\,^3H_2O + \beta^- \rightarrow {}^3H^\bullet, {}^3HO_2^- \ldots \rightarrow {}^3H_2O_2 + 2\,^3H^\bullet. \quad (2)$$

Depending on the storage conditions of tritiated water, in an open or closed container, the concentration of radiolytic oxidizing species and oxygen varies over a wide range, which modifies the corrosion and free potentials of titanium. The $^3HO_2^-$ radical is an ionic intermediate species produced in water radiolysis and diffusing in ^3H_2O with an electrokinetic field. This species is not stable at acid pH. With a concentration of 10^{-2} mol dm^{-3} for $^3H_2O_2$, the corrosion potential is in the prepassive region (−0.5 V/SCE at pH 4). If tritiated water is not stored for long periods in closed containers, the concentration of $^3H_2O_2$ is low, which leads the corrosion potential (−1.3 V/SCE at the same pH) in the active region. The effects of $^3H_2O_2$ and energy released by the β^- particle were reported previously for others materials [5,6].

An acid medium was selected since relatively concentrated nitric acid solutions are produced in tritiated water reprocessing installations during the catalytic gaseous tritium oxidation cycles at 450 °C by air and finely divided palladium. This can be explained by the effect of β^- particles on nitrogen in the air used for oxidation in tritiated water; the reactions are from [1–4]:

$$N_2 + \beta^- \rightarrow 2N^\bullet, \quad (3)$$

$$N^\bullet + 3\,^3HO_2^- \rightarrow {}^3HNO_3 + {}^3H_2O + 2O^\bullet. \quad (4)$$

* Tel./fax: +33 380757610.
E-mail address: gilbert.bellanger@orange.fr
URL: http://corrosion.monsite.wanadoo.fr

0022-3115/$ - see front matter © 2009 Elsevier B.V. All rights reserved.
doi:10.1016/j.jnucmat.2009.01.309

The effects of NO_3^- on corrosion and passivity have been reported previously [6]. Passivity and corrosion depend on the radioactive medium, therefore, the behavior of titanium was studied in the active and passive regions at acid pH and in presence of $^3H_2O_2$ by means of cyclic voltammetry, electrochemical noise and electrochemical impedance spectroscopy. The formation of transient species and their modification at the electrode surface have not been previously studied extensively. Most of these investigations were realized by potentiostatic and potentiodynamic electrochemical methods at low scan rates. In the present work, one of aim very often taken into account is to know the effects of these species through the oxide layer to contribute to the new scientific knowledge. This is explained besides by cyclic voltammetry at high scan rates, electrochemical noise and electrochemical impedance spectroscopy.

2. Experimental equipment with procedures for objective

The voltammetric equipment consisted of a Tacussel bipotentiostat and signal generator (PRT 20 and GSTP 3) connected to a Tektronix 2230 digital oscilloscope. The impedance diagrams were drawn by a Tacussel ZCP 130T controlled by a Hewlett–Packard computer, and using a Hewlett–Packard HP 7440 AXY plotter. Curves were plotted using a titanium disk electrode of 0.2 cm^2 surface. The disk consisted of an industrial titanium rod of 99.5% purity and of commercial availability. The titanium rod was annealed in air at 650 °C for 15 min to remove possible stress in surface. After treatment, titanium was embedded in a Teflon cylinder. In order to avoid infiltration of electrolyte at the titanium/holder interface that often causes random errors in the low frequency data, particular care was taken to make a suitable electrode for impedance and noise measurements. Prior to each use, the disk electrode was mechanically polished using 2000 mesh grade silicon carbide sheets and washed with deionized water. In these conditions, the roughness factor for titanium is estimated to be 1.3. A saturated calomel electrode (SCE) and a platinum electrode were used as reference and counter electrodes, respectively. To avoid capacitive and inductive interferences, a platinum wire was added to the reference electrode with a 0.1 μF capacitance. The sequence in impedance measurements was made in the potentiostatic mode from the lower potentials in the prepassivity to in the first passivity at constant hydrogen peroxide concentration. The frequency range for impedance measurements was from 10 kHz to 10 mHz with a constant AC voltage amplitude of ±10 mV. At high frequency, passive oxide is characterized with surface pH, whereas at low frequency, reactant diffusion into oxide is reached. The frequency was scanned step by step with five steps per decade on a logarithmic scale. Two measurements of AC impedance with Fourier transforms were carried out at each step. A standard procedure was adopted in acquiring the cyclic voltammograms until reproducible values as in the case of the impedance diagrams. The potentials were swept cyclically at a scan rate of 200 mV s^{-1} from the lower potentials in the active region to the end of the first passive region at different hydrogen peroxide concentrations. This method enables to show the dependence of oxide and its different oxidation degrees with local pH on the concentration of hydrogen peroxide and potential. A standard procedure was also adopted in acquiring the electrochemical noise. The data were obtained until reproducible values at different active and prepassive potentials and at different hydrogen peroxide concentrations. Then, electrochemical noise data were computed by spectral method to obtain the phase space portrait for stress organization, by chaotic electrical analyzer to obtain the equivalent electrical circuit, and by surface structure activity analyzer to obtain atomic arrangements. By varying hydrogen peroxide concentration and potential between the active and prepassive regions, instabilities illustrate transitory oxides and stress. Solution pH was measured using a Radiometer Minisis 5000 pH meter. The hydrogen peroxide concentration was controlled by potentiometric measurements.

3. Results and discussion

3.1. Voltammograms and coulometry curves

The use of relatively fast voltammetric scan rates is unusual in corrosion testing, and the justification for this technique is given by Morris and Scarberry [7]. The rapid-scan curves reveal transients peaks where inflections in the slow-scan curves suggest they might exist [8]. Therefore, we have drawn the cyclic voltammograms at a scan rate of 200 mV s^{-1} to demonstrate the behavior of titanium. In the forward scan in Fig. 1(a), the potential is swept over the range of reduction of hydrogen peroxide, in active, prepassive and passive regions up to the second passivity of titanium (Fig. 1(b)) before the return scan. For details, it should be noted that there is no pitting or crevice event in any case after testing in the domain of potentials studied in the Fig. 1(a). In the meantime, it is worth to note there is also no intergranular corrosion in the active region. It was important to verify since we study the behavior of titanium in the active region. For example, it is not the case for a sample sensitized where anodic and cathodic double-loop electrochemical potentiokinetic reactivation tests

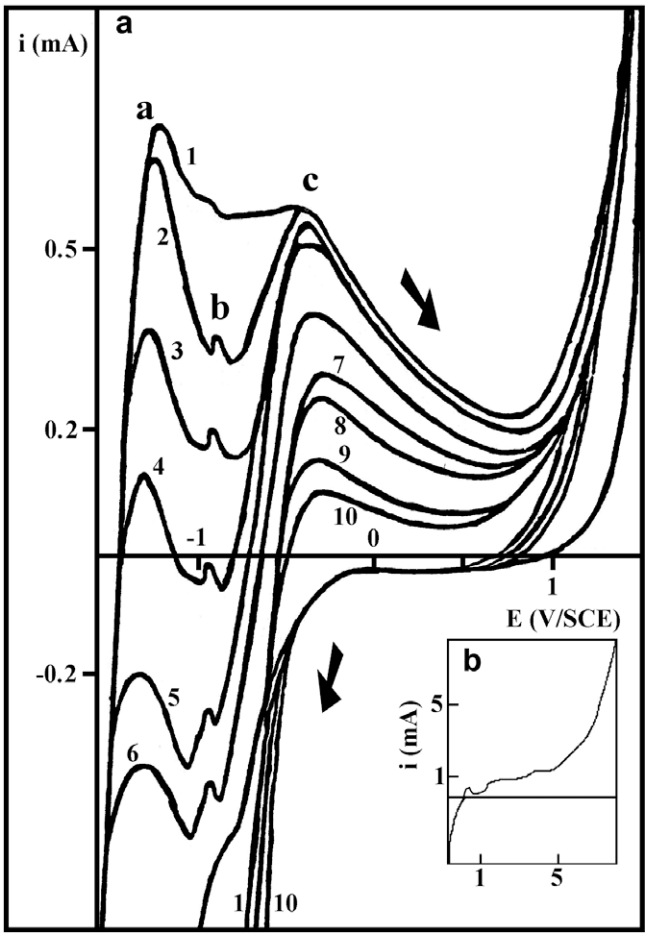

Fig. 1. Voltammetric curves of titanium surface: 0.2 cm^2, scan rate: 200 mV s^{-1}, pH: 4, $^3H_2O_2$: (1) 10; (2) 20; (3) 30; (4) 40; (5) 50; (6) 60; (7) 70; (8) 80; (9) 90; (10) 100 mmol dm^{-3}, (a) view in the active, prepassive and first passive regions, and (b) view in the two passive regions.

were applied [9]. In this case, intergranular corrosion is increasing with the time and the corrosion products during the successive cycles obtained in voltammograms curves (Fig. 2). In this Figure, by integrating the anodic and cathodic active peaks (P_a), it is possible to calculate the ratio of the charges for generalized corrosion and passivation (C_p) and for reactivation corresponding to intergranular corrosion (C_a). In the Fig. 1, interpretation of the voltammetric curves is not simple, and will contribute to scientific knowledge about modifications of oxide, formation of transients in the active peaks and prepassivity. Under these conditions, it can be seen

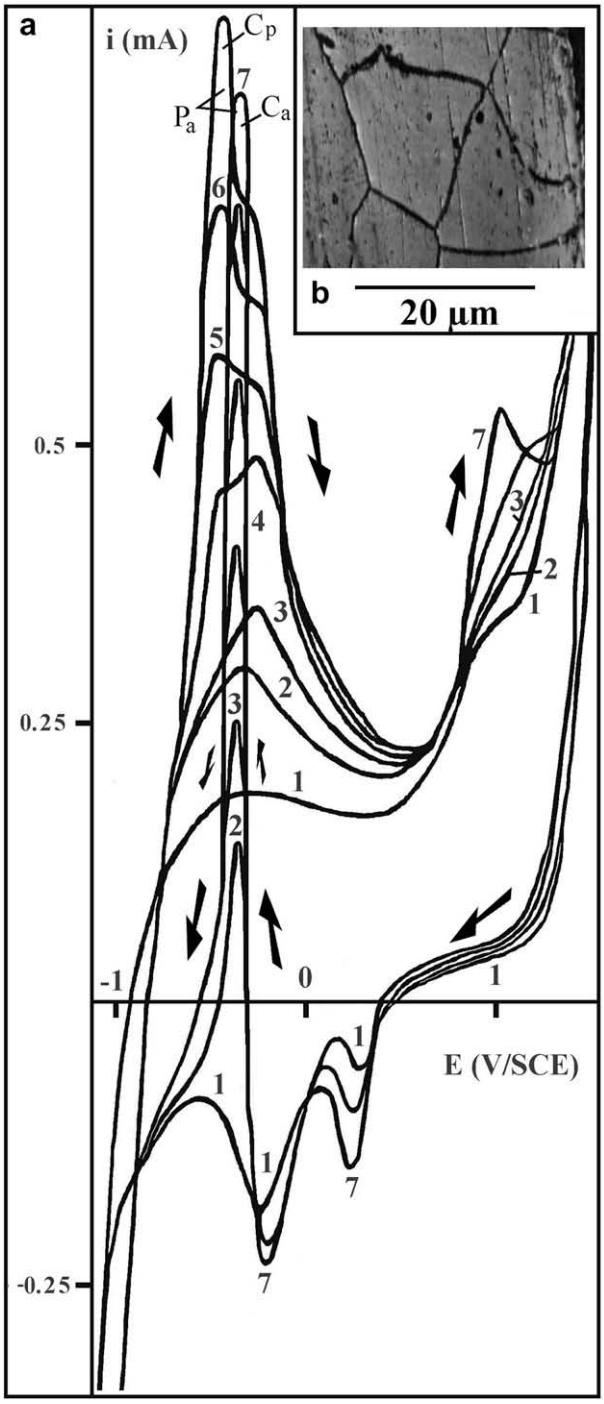

Fig. 2. (a) Voltammetric curves with successive cycles of sensitized metal, surface: 0.2 cm^2, scan rate: 200 mV s^{-1}, pH: 4, and (b) micrography showing intergranular attack.

there are two small peaks (*a*, *b*) at lower potentials due to formation of intermediate oxides in the active region and finally a major peak (*c*) corresponding to a passivating oxide layer essentially formed of TiO_2 which spreads across the surface until at the higher potentials (Eqs. (5)–(15)). Examining the voltammetric curves, the corrosion potential is in the two small peaks indicating instabilities in the active region where the current can be either negative or positive. At the first-second passivity limit (Fig. 1(a) and (b)), the anodic current increases before obtaining the plateau of second passivity in Fig. 1(b). The scan in Fig. 1(a) depends on the concentration of hydrogen peroxide, e.g., on the intermediate species and oxidation mechanisms in the active to passive regions. The anodic peaks (*a*, *b*) of around −1.3 and −0.8 V/SCE correspond to the formation of intermediate layer of $Ti^{II}O^3H^+$ and $Ti^{III}OO^3H$ with $Ti^{III}O^+$. McCafferty et al. [10] explained the peaks in terms of uppermost oxide monolayer. The formation of hydroxide (Eqs. 6, 8, 9, and 12) may also be related to form an outermost layer. Expanded scans giving current vs. time (Fig. 3) obtained by loading PeakFit™ program and taking account the current of hydrogen peroxide reduction show that the peaks *a* and *b* vary inversely and indicate transients are dependent of the oxidizing radiolytic media. Table 1 gives the corresponding electric charges (*Q*) under each peak of transients. Using this potentiodynamic method, charges depend on the hydrogen peroxide concentration showing a catalytic effect of the media aiding the formation of Ti^{III} then TiO_2.

Titanium is assumed to form intermediates, and processes are discussed by Newman et al. [11] and Galland et al. [12]. From the investigations of these authors, the proposed anodic reaction scheme at acid pH is:

Active range

First step- formation of Ti^{II}:

$$Ti \rightarrow Ti^{2+} + 2e^-, \tag{5}$$

$$Ti^{2+} + 2\,{}^3H_2O \rightarrow Ti^{II}O^3H^+ + {}^3H_3O^+, \tag{6}$$

$$Ti^{II}O^3H^+ + {}^3H_2O \rightarrow TiO + {}^3H_3O^+, \tag{7}$$

$$Ti^{II}O^3H^+ + 2\,{}^3H_2O \rightarrow Ti(O^3H)_2 + {}^3H_3O^+. \tag{8}$$

Second step- Ti^{II} is oxidized in Ti^{III}:

$$Ti^{II}O^3H^+ + 3\,{}^3H_2O \rightarrow Ti^{III}OO^3H + 2\,{}^3H_3O^+ + e^-, \tag{9}$$

$$2TiOO^3H \rightarrow Ti_2O_3 + {}^3H_2O, \tag{10}$$

$$Ti^{III}OO^3H \rightarrow Ti^{III}O^+ + O^3H^-. \tag{11}$$

Prepassive and passive layer formation range:

$$Ti^{III}O^+ + 4\,{}^3H_2O \rightarrow Ti^{IV}O(O^3H)_2 + 2\,{}^3H_3O^+ + e^-, \tag{12}$$

$$Ti^{IV}O(O^3H)_2 + 2\,{}^3H_3O^+ \leftrightarrow Ti^{IV}O(O^3H)_2 2\,{}^3H^+ + 2\,{}^3H_2O, \tag{13}$$

$$Ti^{IV}O(O^3H)_2 2\,{}^3H^+ + {}^3H_2O_2 \rightarrow TiO_2 + 2\,{}^3H_3O^+, \tag{14}$$

$$TiO_2 + 2\,{}^3H_3O^+ \leftrightarrow (TiO_2)2\,{}^3H^+ + +2\,{}^3H_2O. \tag{15}$$

In these equations, Ti^{II} and Ti^{III} are unstable in hydrated medium, only Ti^{IV} is stable [10]. Eqs. (13) and (15) show that there is intercalation of local protons at the surface Ti^{IV} sites. It is of interest to comment the passivity where the current is limited by O^{2-} diffusion within the passive oxide. Some oxygen atoms may be adsorbed on the oxide, and then these atoms diffuse into oxide via O^{2-} ions (Eq. (16)) or are reduced in ${}^3H_2O$ at the surface of oxide as indicated by Pleskow [13] and Randin [14]. Ion diffusion in the electrochemical interface is assisted by the local electrical field.

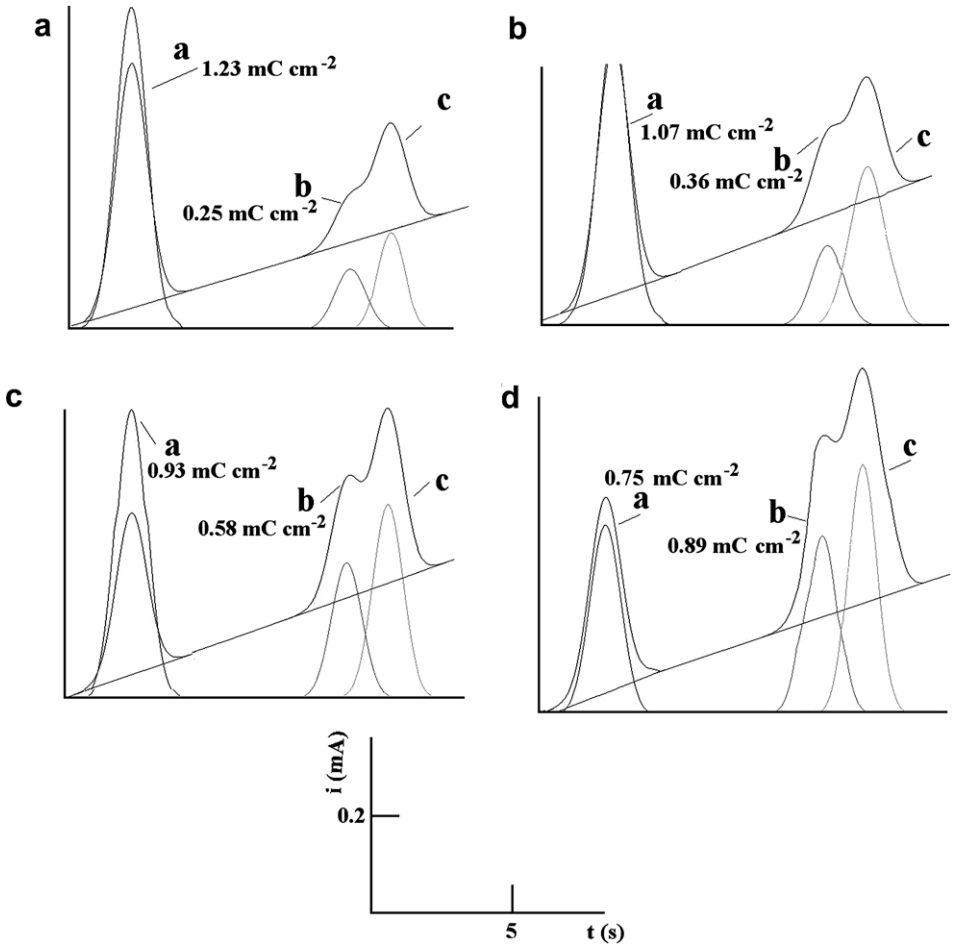

Fig. 3. Expanded voltammetric curves of titanium in active region surface: 0.2 cm^2, scan rate: 200 mV s^{-1}, pH: 4, $^3H_2O_2$: (a) 10; (b) 30; (c) 70; and (d) 100 mmol dm^{-3}.

Table 1
Values of the electric charges during anodic oxidation under the peaks *a* and *b* as a function of hydrogen peroxide concentration.

$^3H_2O_2$ (mmol dm^{-3})	10	30	70	100
Q (mC cm^{-2} Ti^{II})	1.23	1.07	0.93	0.75
Q (mC cm^{-2} Ti^{III})	0.25	0.36	0.58	0.89

$$O_{ads} + 2\,e^- \rightarrow O^{2-}. \quad (16)$$

The reactions in Eqs. (5), (9), and (12) are successive electrochemical systems with a mono or multi-layer formation. The active peak potential (*b*) corresponds to the position of a shoulder at lower hydrogen peroxide concentration (curve 1). According to Eqs. (6), (7), (8), (9), (12), (13), (15) where hydroxonium ions are produced for the production of Ti^{II-IV}, and also the slight shift of potential in the peak *c* in Fig. 1, local pH is more acidic. This is more easily evidenced by controlling variation of the acid pH in the electrode surface. Therefore the tritiated water–titanium interface is acidified during the scan in activity, prepassivity and passivity. These results indicate that passivity is dependent on the species and the precursor oxides on the surface of titanium in the active region, the local increase in $^3H_3O^+$, and the presence of hydrogen peroxide. These modify the electrochemical activity in the tritiated water–titanium interface for prepassivity and passivity. This also indicates that the processes at the surface are highly dependent upon diffusion through the oxide interface by Eq. (16). The $^3H_3O^+$ concentration, precursor oxides, hydrogen peroxide and hydrated oxide are responsible for the characteristics of passive oxide. Integrating the current in the expanded scans, the coverage rate by transitory oxides as calculated by MacDonald and Roberts [15] and Calandra et al. [16] and MacDonald and Roberts [15] is 0.85, whereas recovery is total when integrating all passive current for TiO_2. The partially hydrated precursor oxides (Eqs. (5)–(11)) undergo a structural rearrangement along with an electron transfer. These adsorb in the form of monomolecular layers on the surface. Instead of just molecular adsorption, the precursor species often also anchor to the surface by reacting with the surface group. The adsorbed layer will be converted to an oxide via successive surface reactions between the metal and with the hydrogen peroxide. SIMS and XPS examinations realized by E. McCafferty, et al. [10] show that the outermost oxide is essentially formed of TiO_2, but it also contains the transients $Ti^{II}OH^+$ and $Ti^{III}O^+$. The signal of $Ti^{II}OH^+$ is more intense than that of $Ti^{III}O^+$, indicating that the surface retains OH^- species for a concentration of 10 OH^- nm^{-2} and a depth of a few nanometers. In the inner oxide, the ratio $(Ti^{II}OH^+)/(Ti^{III}O^+)$ decreases with depth, indicating that hydroxyl species are the constituent of the outer oxide layer. In the more inner oxide, the $Ti^{III}O^+$ signal is about ten higher than the $Ti^{II}OH^+$ signal, indicating that this region does not contain hydroxyl groups. The orientational plane might be visualized by looking the atomic arrangement in Fig. 4 based on the oxide film. Films of TiO_2 have interesting properties such as good chemical resistance and relatively high dielectric constant. It exist several polymorphs, but the more stable phases are the rutile and anatase phases with tetragonal structures (Fig. 4(a)). The TiO_2 film grows with a strong texture and an electron transfer very low.

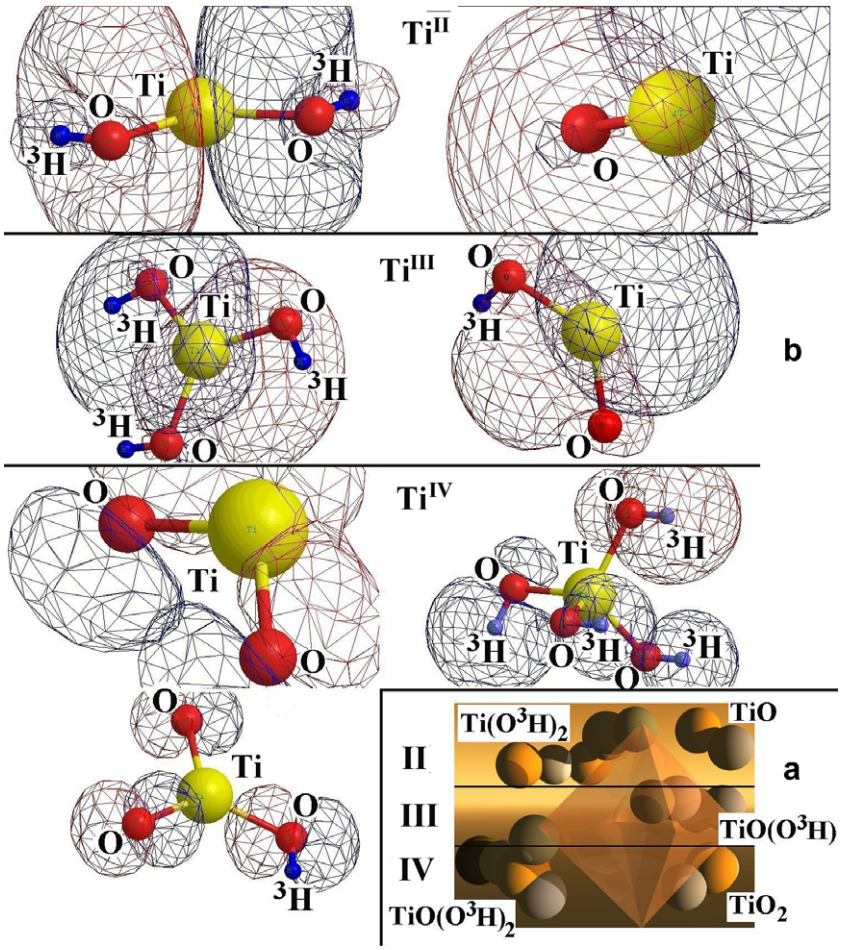

Fig. 4. (a) Tetragonal structure of TiO_2, and (b) simulation of the atomic arrangement for stable and unstable oxides (Ti^{II}, Ti^{III} and Ti^{IV}).

In order to modeling the adsorbed precursor oxides, we have numerically analyzed and carried out calculations to obtain the characteristics, the size and the structural aspect of these species in presence of hydrogen peroxide and hydroxonium ions using the Chem-Office™ program. During the last years, considerable effort has been spent on solving the structure of adsorbed layers. Achievement in this matter is well illustrated by a handbook containing a catalogue of these structures [17] and database can be obtained using a graphic program [18]. As an example, structures of Ti^{II}, Ti^{III} and Ti^{IV} are shown in Fig. 4(b). This Figure schematizes the adsorbed main species and the oxide layer. These species produce orbitals, and the considered surface and volume have been modeled lying in parallel the adsorbed layer to the oxide surface in order to get a reasonable coverage. TiO_2 overlaps the adjacent adsorbed titanium hydroxides and fills the different orbitals for transients. Calculations using the MerckIndex™ database give the bond lengths and angles for these different species in minimizing energy and taking into account the $^3H_3O^+$ ions. Results are reported in Table 2. In this Table, it can be seen that the bond angles and the bond lengths of Ti^{II} and Ti^{III} differ to these obtained with TiO_2. Ti^{II} and Ti^{III} have the tendency to increase the bond length of Ti–O whereas the bond length is constant for the hydroxide radical in any case. Increasing the bond length, decreases the bond and adsorption strengths, and consequently the corresponding driving force is less important than this obtained with Ti^{IV} linked to O^{2-} in the form TiO_2. It can be deducted from the results that $Ti^{II}O^3H^+$ is limiting adsorption of hydroxide ion in $Ti^{III}OO^3H$ at low $^3H_2O_2$ concentration (Tables 1 and 2), and Ti^{II} with Ti^{III} are less stable than TiO_2 favoring diffusion of O^{2-}. Diffusion of O^{2-} favors oxide growth. According to the Chem3D software, the lattice size of the Ti^{II} and Ti^{III} species undergoes expansion in regard to that of TiO_2 so that texture in the interface is adjusted with constraint and stress depending on transitory oxides. Consequently, the strong texture within oxide will be an important parameter.

Table 2
Bond lengths and angles of unstable and stable species for Ti^{II}, Ti^{III} and Ti^{IV}.

	Ti^{II}	Ti^{III}	Ti^{IV}
Bond lengths (Å)			
Ti–O	31.9	116.4–121	29.6
O–^{3}H	0.94	0.96	0.94
Bond angles (°)			
O–Ti–O	2.5	141.6	119.4
Ti–O–^{3}H	162–174	174.4	158–172

The currents observed in the active, prepassive and passive regions are attributed to the double layer, the capacitive oxide charging current and the faradaic current. The double layer capacitance obtained by impedance measurements in the subsequent part is about 50 μF cm^{-2} over the potential range, thus the double layer charging current should be no greater than 2 μA at 200 mV s^{-1}. Therefore the currents observed in the voltammetric curves are principally due to the intermediates and passive oxide formation. It is known that the anodic oxide films on titanium have *n*-type semiconductive properties in the first region of passivity, whereas in secondary passivity, oxide is a dielectric layer. Between the two regions, property of the oxide film is a *n*-type semiconductor with

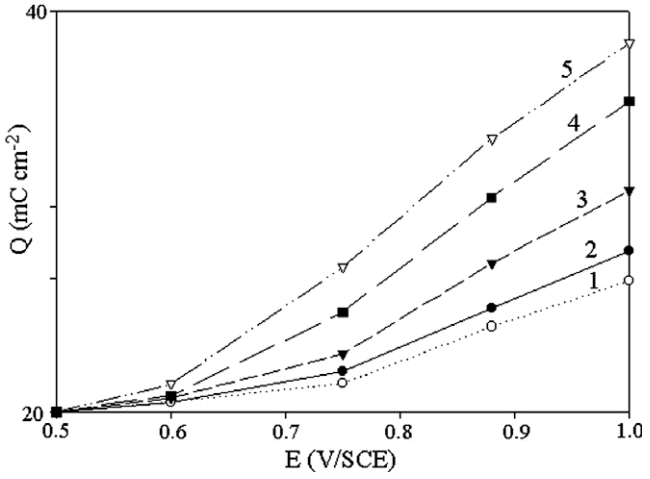

Fig. 5. Linear relationship between the electrical charge and potential at the end of the first passivity for oxide, $^3H_2O_2$: (1) 10; (2) 25; (3) 50; (4) 75; and (5) 100 mmol dm^{-3}.

an outer dielectric layer [19]. Using the potentiostatic mode until the steady-state current by coulometry technique to obtain the electrical charges during oxide growth from the higher potentials in the first passivity, it is found that the sum of charge increases with the hydrogen peroxide concentration and potentials (Fig. 5) until the passive state on titanium (TiO_2) could be regarded as a steady-state. This Figure showing a linear part between the charge (Q) and the potential with hydrogen peroxide concentration enables to write:

$$Q = KE + b \tag{17}$$

where K is the slope, b the intercept of the linear part and E the applied potential during thickening determined from the intercept. According to Faraday's law, the steady-state film thickness, d, can be represented by:

$$d_{sc/di} = QM/nF\rho \tag{18}$$

where M is the considered oxide molecular weight (79), n the mean number of electrons required to form one molar of oxide at the oxide/tritiated water interface (4), the subscript sc/di indicates the probable semiconductor and dielectric behavior and ρ the density of oxide (3.2 g cm^{-3}). Thus, the linear correlation between the steady-state oxide thickness and potential can be obtained by substituting Q and expressed as:

$$d_{sc/di}\frac{M(EK+b)}{nF\rho}. \tag{19}$$

Consequently, $\partial d/\partial E$ is equal to $KM/nF\rho$. In application, variation of oxide thickness in the end of first passivity and with high $^3H_2O_2$ concentration is about 12 nm V^{-1}, whereas at low concentration, variation is 5 nm V^{-1}. As an example, thickness at high $^3H_2O_2$ concentration is about 25 nm. These results enable us to show the influence of hydrogen peroxide concentration in this region of potential.

When the anodic oxide film is of mixed properties, a high electric field across the space charge layer. According to the point defect model theory as proposed by MacDonald [20] and Bessone et al. [21] to describe the characteristics of passive films on metals, the electric field strength within the film is constant during film growth, but will depend on the hydrogen peroxide concentration and weakly vary on depth of thickness due to the mixed charges. The variation of field strength in V cm^{-1} may be calculated from the following equation [22]:

Table 3
Values of the electric field strength and of stress as a function of hydrogen peroxide concentration during anodic oxidation in the end of the first passive region ($\Delta\Phi$) and in the prepassive–passive region ($\Delta\chi$).

$^3H_2O_2$ (mmol dm^{-3})	10	25	50	75	100
$\Delta\Phi$ (MV cm^{-1})	0.4	0.32	0.2	0.15	1
$\Delta\chi$ (Pa)	7.8	5.6	3.2	2.4	1.6

$$\Delta\Phi_{sc/di} = \left\{\frac{1-\frac{RT\partial\log I}{nF\partial E}}{\frac{KM}{nF\rho}}\right\}_{^3H_2O_2}. \tag{20}$$

where I is the steady-state current in the higher potentials for the first passivity obtained during integrating the charges in the potentiostatic mode (Fig. 5). Table 3 gives the values of the electric field strength across the oxide film, calculated by using Eq. (20). The electric field strength exhibits an increasing tendency with increasing hydrogen peroxide concentration. This behavior and high values signify that electron transfer is very low and TiO_2 grows with a strong texture and probably with a marked dielectric behavior in the higher potentials. Considering oxide as a parallel-plate capacitor, capacitance is about 5×10^{-8} F cm^{-2}. This very low value would signify presence of semiconductor and dielectric layers. When the part of the dielectric layer is reconverted to a semiconductor layer at lower potentials, positive charge donor states become available to form the space charge layer in the film. In this case, the donor density (n_d) can be determined from equation:

$$n_d = \frac{2\varepsilon\varepsilon_0\Delta\Phi_{sc/di}}{ed}. \tag{21}$$

where ε is the relative dielectric constant of oxide (75), ε_0 the permittivity of free space (8.9×10^{-14} F cm^{-1}), e the electron charge (1.6×10^{-19} C) and considering a thickness of 25 nm. The donor density is 9×10^{18} carrier cm^{-3}. This result confirms that transfer is very low in TiO_2 when the potential is at the limit of the first and second passivity. These results and subsequent values will indicate the presence of semiconductor and dielectric layers.

3.2. Impedance diagrams

This section is concerned with the analysis of impedance spectra obtained at the higher $^3H_2O_2$ concentration and at different potentials in the range of lower passive potentials in the first passivity. These potentials were swept in a nobler direction step by step after the titanium was passivated in the first applied potential. In the passive domain, the semicircles in the experimental Nyquist plots are too incomplete over all the frequency range to be easily interpreted, therefore the Bode plots were drawn. Comparative measurements (Fig. 6) show changes in log $|Z|$ and phase angle vs. log (f). In this figure, f is the frequency, $|Z|$ the impedance module and θ the phase angle. The Bode plots are characterized essentially by two distinct regions. In the higher frequency region (10–100 kHz), the Bode plot exhibits a constant (horizontal line) log $|Z|$ value vs. log (f) with phase angle values near 0°. This is the response of the electrolyte resistance R_{el} (resistive region), which can be neglected with respect to the interfacial impedance. The region in less high frequency corresponds to the double layer charging current. The double layer capacitance (C_{dl}) stands for the interfacial capacitance with the transfer charge resistance (R_{ct}). In the broad low and middle frequency range, the diagrams display a linear slope of about −0.8 in log $|Z|$ as log (f) decreases, while phase angle values approach −75°. This characterizes the response of a passive oxide capacitance. Dispersion in impedance module and phase angle is obtained below 10^{-1} Hz. This can be attributed to the possible presence of Ti^{II} and Ti^{III} in the TiO_2 layer.

Based on this description of the system, the electrochemical impedance spectra were simulated, and the equivalent electric cir-

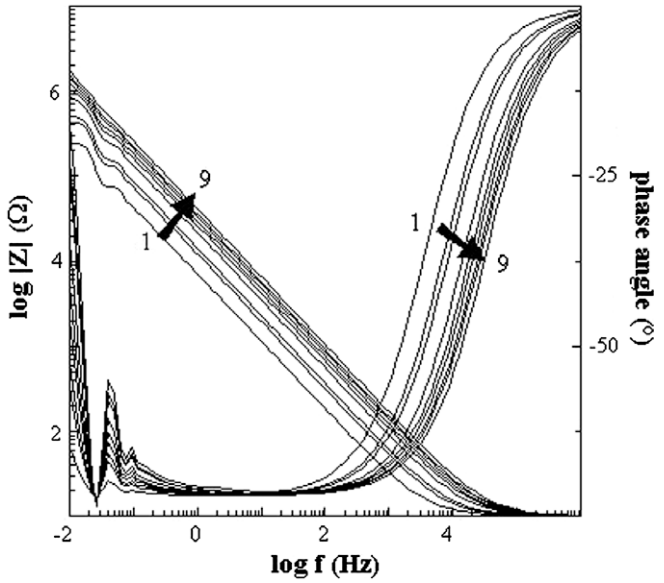

Fig. 6. Bode diagrams for titanium in prepassive–passive region. surface: 0.2 cm^2, pH: 4, potential effect: (1) −0.36; (2) −0.34; (3) −0.32; (4) −0.30; (5) −0.28; (6) −0.26; (7) −0.24; (8) −0.22; (9) −0.20 V/SCE, 100 mmol dm^{-3} $^3H_2O_2$.

cuit is depicted in Fig. 7 according to [23]. From the equivalent circuit, the calculated parameters were analysed. The middle two branches of the electrical circuit correspond to the electronic transfer at the interface, which is considered to be dominated by the electric properties of the oxide layer in means of an oxide resistance (Rox) with a diffusion impedance (W) and an oxide capacitance represented by the constant phase element (CPE). The CPE impedance is defined as:

$$Z_{CPE} = A(2j\pi f)^{-\alpha} \tag{22}$$

in which, α is a parameter between 0 and 1 for the experimental and simulated diagrams, $j = \sqrt{-1}$, and A the frequency-independent constant related to the oxide layer capacitance. When α is near 1, the impedance of constant phase element corresponds to a pure oxide capacitance. The Warburg diffusion impedance (W) is due to the possible diffusion of species in micro-pinholes in the surface of oxide, diffusion is represented by the coefficient σ [24], as represented in Eq. (23).

$$|W| = \sigma\omega^{-0.5}(1-j) \tag{23}$$

where ω is the angular frequency. High value of σ, corresponds to a blocking character of oxide. On this basis, the calculated values of C_{ox} are given as a function of potentials in Table 4. The spectra displays a high corrosion resistance in high $^3H_2O_2$ concentration and in passive potentials as it was expected by the high values of R_{ox}

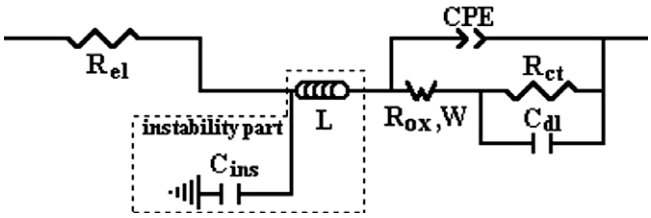

Fig. 7. Equivalent electric circuit to simulate the results obtained by electrochemical impedance spectroscopy. R_{el}, R_{ct} and R_{ox}: electrolytic, charge transfer and oxide resistances with a diffusion impedance (W), C_{dl}, CPE: double layer capacitance and constant phase element representing the oxide capacitance (C_{ox}), L and C_{ins}: elements of the electrical circuit introducing instabilities (in the dashed part).

Table 4
Dependence of oxide capacitance on the prepassive–passive potentials and at high hydrogen peroxide concentration.

E (V/SCE)	−0.400	−0.380	−0.360	−0.340	−0.320	−0.300
C_{ox} (μF cm^{-2})	8.6	8.0	7.6	7.1	6.7	6.0

(0.2 MΩ cm^2) and the capacitive value of C_{ox} (about 6×10^{-6} F cm^{-2}). Thickness is about 11 nm. The variation of C_{ox} indicates that the oxide layer formation obeys a law depending on the potentials as indicated by Schmuki and Böhni [25]. A 'critical capacitance' corresponding to its lower value denotes the perfect semiconductor oxide layer. Calculation obtained by the simulation program for the equivalent circuit, showed that both the α parameter and the Warburg diffusion coefficient are lower when oxide growns at lower potentials. While the lower Warburg coefficient indicates less insulating oxide, the α values should be related with the formation of metastable oxides [26] with presence of transients as $Ti^{III/IV}$ in the outer layer when potential decreases. It is also possible in this case that the electrical circuit takes account of the undetermined circuit elements (dashed lines) related to the electrochemical chaos processes occurring at the interface. The oxide has a significantly lower blocking character than this obtained at the end of the first passivity, such results can be explained by a less stable nature.

The Bode plots (Fig. 6) allow us to calculate the flatband potential (V_{fb}) and the donor density (n_d) for this region following the Mott–Schottky equation:

$$C_{ox}^{-2} = \frac{2\Delta E}{en_d\varepsilon\varepsilon_0} + \frac{d_{sc/di}}{\varepsilon\varepsilon_0}. \tag{24}$$

Assuming that additional capacitive elements such as the Helmholtz layer capacitance and the dielectric layer ($d_{sc/di}$) can be neglected in this potential region, a linear slope is observed between −0.4 and −0.3 V/SCE (Fig. 8). The donor density which corresponds

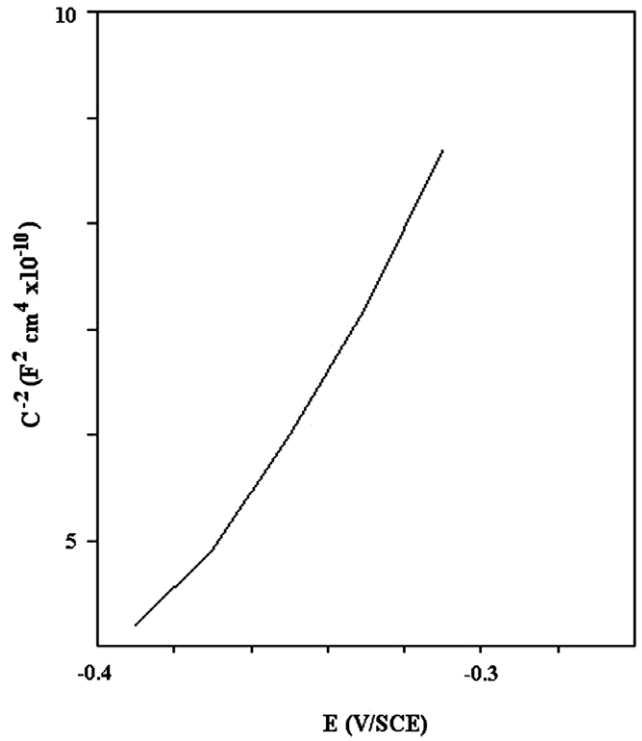

Fig. 8. Change in capacitance C^{-2} during a potential sweep with 100 mmol dm^{-3} $^3H_2O_2$.

to Ti^{4+} and Ti^{3+} cations in oxide is 2×10^{20} carriers cm^{-3}. Deviation in value of donor density and capacitance in the prepassive–passive region in comparison to this in the transition region before the second passivity can be explained in term of a semiconductor layer with continuous transformation followed of partial annihilation during polarization if scanned at the higher potentials towards the end of first passivity in forming a dielectric layer and a semiconductor layer. Therefore, formation of the dielectric layer is essentially accompanied by the high electric field applied in the film at the higher potentials. The conversion of the pure *n*-type semiconductor to dielectric layer causes a change in the potential distribution in the film, as shown in Fig. 9. The electric field in the dielectric layer is uniform, whereas it varies with depth in the semiconductor layer [19]. According to Azumi and Seo [19], the donor states in the *n*-type TiO_2 are thought essentially to be Ti^{3+} states which emit free electrons with intercation of local protons at the surface. Under the electric field applied in the oxide, free electrons and charged Ti^{3+}, Ti^{4+} donors are spatially separated to form the space charge in the film. The flatband potential extrapolated to the potential axis is close to −0.38 V/SCE as estimated from Fig. 8. It appears to be 120 mV above the corrosion potential at high hydrogen peroxide concentration, it will be strongly depending on pH according to Eqs. (6)–(15) and in [6]:

$$V_{fb} = b - 0.06c\ \mathrm{pH}. \tag{25}$$

Therefore it is depending on the local proton adsorption–desorption equilibrium at the oxide-tritiated water interface. On going from positive to negative potentials in the flatband region, no reversal of the electric field was observed as might be expected from depletion to an accumulation layer in electron in the conduction-band filling state [19]. The observed result is consistent with charge compensation by intercalation of local protons to compensate the electron trapped at the surface Ti^{IV} sites as represented by Eqs. (12)–(15), (27)–(29):

$$Ti^{IV}O(O^3H)_2 2^3H^+ + 2e^- \rightarrow \left\{Ti^{IV}O(O^3H)_2^3H_2\right\}_{oxide}, \tag{26}$$

$$(TiO_2)2^3H^+ + 2e^- \rightarrow (TiO_2^3H_2)_{oxide}, \tag{27}$$

$$(O^{2-} + 2^3H^+)_{oxide} \leftrightarrow (O^3H^-)_{oxide} + {}^3H^+ \leftrightarrow (O - {}^3H_2)_{oxide}. \tag{28}$$

O^3H^- formed by Eq. (29) and free electrons (Eqs. (27), (28)) compensate the positive charge of the donor state (Ti^{3+} and Ti^{4+}) and annihilate the space charge causing dehydration of oxide (Eq. (29)) by pulling out hydroxyl ion and proton under the high electric field, this process leads to dielectric layer formation [19]. Moreover, as V_{fb} depends on the surface charge, these equilibria determine the onset potential with pH for charge accumulation in TiO_2. In this context as showed by Boschloo and Fitzmaurice [27], calculation indicates that the total density of titanium atoms in surface is about 5×10^{14} atom cm^{-2}, and titanium atoms acting as trap for electron is 2×10^{13} atom cm^{-2}, in short 4% of titanium atoms acts in this trapping process and the oxide film should contain bound water in the outermost part.

3.3. Electrochemical noise

Unstable oxide will induce compressive or tensile strength in the film. If strength exceeds a value, stress is created in the oxide. Ueno et al. [28] reported that the stress of anodic oxide films depends on the potential of film formation, the nature of film and the kind of electrolyte used during anodic oxidation of metal. The other factors influencing the stress of anodic oxide films are texture, crystallization of film and dehydration of a hydrous film during anodic oxidation as showed by the 4% Ti atoms in Eqs. (27)–(29) [29–31]. Tensile and compressive molar volume can also explain stress, considering the molar volumes of oxides Ti^{IV} (24.7 $cm^3\ mol^{-1}$) and of $Ti^{II/III}$ (53.1 $cm^3\ mol^{-1}$), fineness ratio is 2.15 between the region of transients and TiO_2 formation. It can be expected that changes in volume by transients contribute to stress in oxide. Stress, $\Delta\chi$, generated during anodic formation of the oxide film can quantitatively be measured by the Butler' method [32]. In order to have access to valuable information on the stress fluctuation in surface corresponding to elastic deformation, computer programs have been devised. The compressive stress to the plane of a oxide film can be calculated by using a simple parallel-plate capacitor model as follows.

$$\Delta\chi = \frac{\varepsilon\varepsilon_0(\Delta\Phi)_{sc}^2}{2d^2} \tag{29}$$

where $\Delta\Phi_{sc}$ is the difference of potential in the space charge layer, which is equivalent to the difference between the corrosion potential and the flatband potential. Values calculated as a function of the hydrogen peroxide concentration are shown in Table 3. $\Delta\chi$ decreases with increasing the hydrogen peroxide concentration in the prepassive to passive region. This decrease means stress release in presence of stable TiO_2 and hydrogen peroxide, and may be ascribed to a stable activity with less transients at high $^3H_2O_2$ concentration.

The changes in stress of oxide can also be measured qualitatively by electrochemical noise method. The study of processes of unstable oxide by electrochemical noise involves the monitoring and analysis of spontaneous current or potential fluctuations recorded as a function of time [1–3]. In this technique, oxidation of titanium was performed from the active region to the prepassive region letting the potential free to vary within an amplitude of 10 mV. The fluctuations in the potential obtained for Ti^{II}, Ti^{III} and TiO_2 formation are shown in Fig. 10. Graphs in this figure depicts three types of signal: (i) random and chaotic for Ti^{II} and Ti^{III} and illustrate stress and instability in oxide layer ((a)–(b)). This is confirmed by the corrosion potential which cannot correctly defined in the voltammetric curves. Species of Ti^{II} and Ti^{III} types are not stable. (ii) in the case of TiO_2, oscillations are periodic ((c)–(d)). In passivity, oscillations disappear, this indicates stabilization in the TiO_2

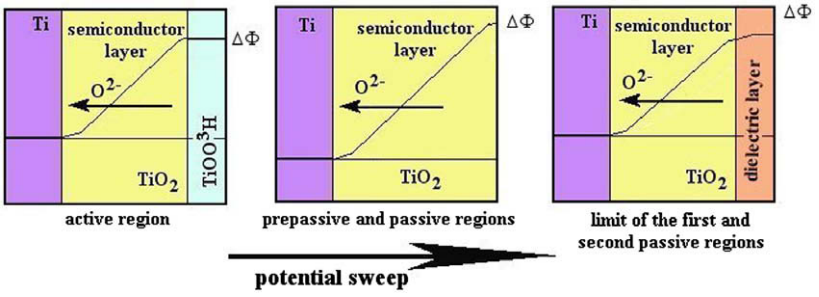

Fig. 9. Simplified elementary steps involved in transformation of oxide layers in function of species in different regions of passivity and in presence of hydrogen peroxide.

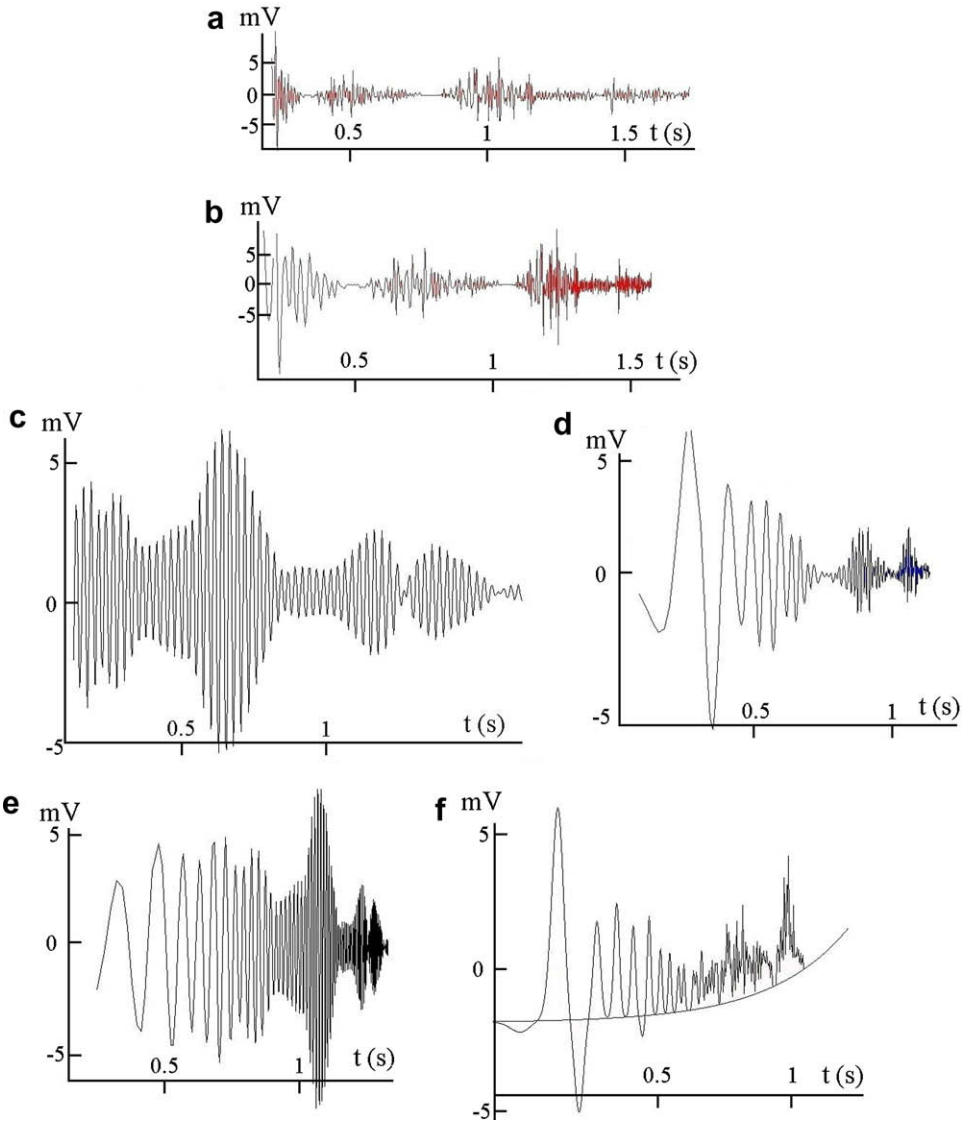

Fig. 10. Plot of data acquired during fast growth events in presence of hydrogen peroxide in the active region showing instabilities in potential. (a)–(b) Random signal (−1.0 V/SCE), (c)–(d) periodic signal (−0.65 V/SCE), (e)–(f): semi-periodic signal (−0.75 V/SCE).

form. (iii) both random and chaotic behavior with periodic signal illustrate electrostress and stability coupled in oxide ((e)–(f)).

Another procedure for the mathematical treatment of electrochemical noise measurement has been implemented using the spectral method and the phase space portrait [33]. In this case, noise has been monitored using ChaoticMapper™ and ChaosDataAnalyzer™ programs. The spectral analysis estimates the power spectral density for the potential fluctuations, that is, the distribution of the power of the signal in the frequency domain. Spectral analysis using the fast Fourier method transforms the time series of noise signal into a frequency range dependent on the sampling rate and the number of analyzed data records. This analysis offers an interpretation of the electrochemical noise based on estimating the stochastic (non periodic and chaotic systems) and deterministic features of the system. The shapes of the noise can be used to discriminate between passivity and stress. In this case, the probability of unstable oxide should increase with the presence of the inclusions of Ti^{II} and Ti^{III} at lower potentials and decrease with the addition of hydrogen peroxide aiding the Ti^{IV} formation. The aim of this present part is therefore to measure the noise generated by these inclusions and to analyze the data utilizing power spectral densities with a stochastic method. In this objective, the electrochemical noise analysis is achieved by transforming the individual positive and negative fluctuations into basic events to give peak duration times.

With decreasing potential and hydrogen peroxide concentration, the chaotic oscillation frequency and stress increase (Fig. 10 and Table 3). These oscillations are due to the nucleation of unstable species in active and prepassive regions and repair process associated with the propagating stress [28,34] and changes in the composition of the oxide surface. Stress of the oxide layer is caused by non stable Ti^{II} and Ti^{III} presence in oxide [10], whereas stable oxide layer is caused by total Ti^{IV} formation. The initiation of stress occurs only for sufficient amounts of Ti^{II} and Ti^{III}. Also, it is recognized that the ability to produce a passive layer depends on the concentration of hydrogen peroxide. At high concentration of hydrogen peroxide, it has been remarked that the events are cyclic and periodic before to disappear, this indicates stabilization in the passivation process. In this perspective, the phase space portrait obtained by intelligent instrumentation depicts three types of signal characterized by random or chaotic, semi-chaotic and periodic noise depending on birth and death of stress or passivity,

suggesting that the system is driven by two dimensional dynamics. Starting at zero, successive segments of about 1500 data points were extracted from the time series for analysis in steps of potentials and hydrogen peroxide concentration. In the random behavior, there is a short number of time sequences, and in the semi-periodic or periodic behavior, the time sequences are larger. Using the chaos programs, the phase space portrait was constructed using its derivative. The periodogram in Fig. 11, is the frequency representation of the information displayed in the time domain determined by an autocorrelation function where τ is an arbitrary time constant whose practical choice is not trivial. Each point in this space represents a state of the system. Joining the successive state points by a continuous curve gives the trajectory filling the phase space. Physically, the autocorrelation function quantifies how regular a random process is. The two cases are the noise and the sinusoid. Each value of a noise sequence is completely independent of all others. Contrarily, a sinusoid is perfectly regular with a period. Graph of derivative versus time-delay (Fig. 11(a–d)) for random oscillations produces a plot with discernible structure in form of elongated core toroid indicating an unstable system [34]. In Fig. 11(e–g), the trajectory of system spirals into the orbits and converges to the center of toroid then turns back in the external rolled orbit indicating that process leads to a stable system. In Fig. 11(h–j), the portrait of derivative suggests two types of mixed-mode oscillations: chaotic and periodic systems which are represented by centered orbits consisting of a core toroid and rolled orbit where aspect has been reported by various authors [35–37]. In this case, graphs represent repair process associated with the propagating stress. These orbits can topologically be regarded as a pattern reinforcing the idea that topological analysis of the phase space is fruitful to reveal the level of organization of unstable and stable systems and to interpret the dynamic implied in unstable oxide formation [38]. In fractal measurements, the Lyapunov exponent is a measure of the rate at which trajectories in phase space converge. Chaotic orbits have positive Lyapunov exponents (Fig. 11(a–d)). In periodic orbits, Lyapunov exponents are negative (Fig. 11(e–g)). Convergence of the toroid and rolled orbit (Fig. 11(h–j)) reveals the Lyapunov exponents values of −0.95

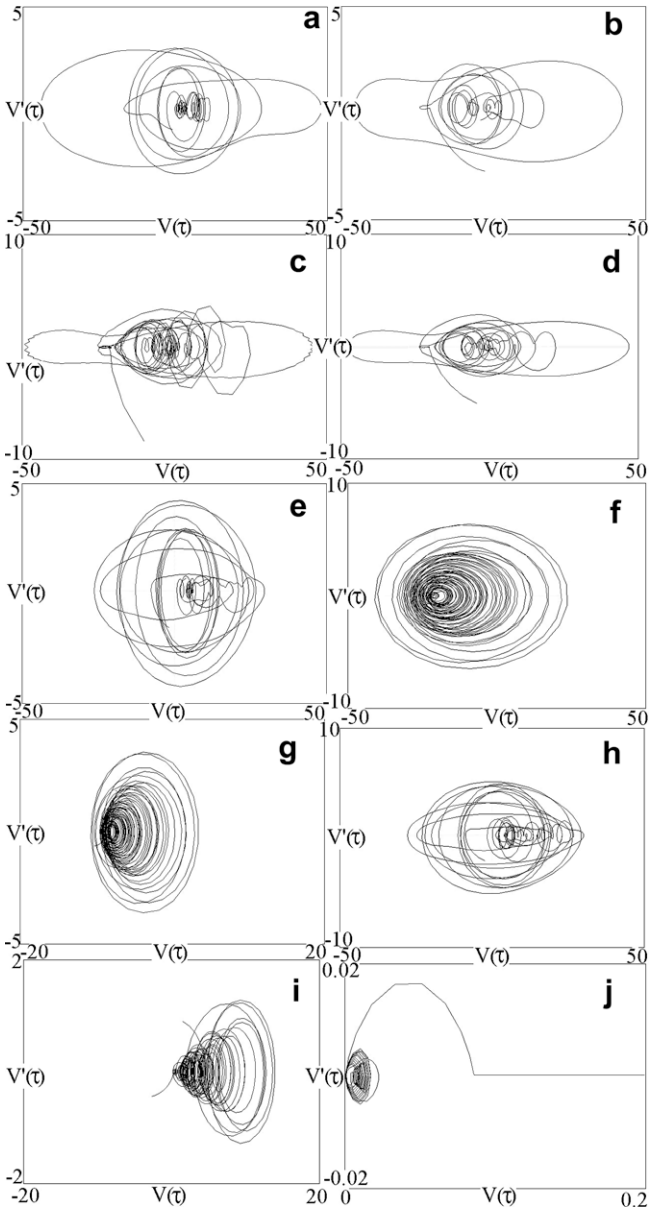

Fig. 11. Graphs of data of phase space plots for potential instability analysis given for $V(\tau)$ versus the time-decay and the derivative $V'(\tau)$. $V(\tau)$ is the potential according to Fig. 10. (a)–(d) elongated core toroids obtained for −1.0 V/SCE, (a) high $^3H_2O_2$ concentration; (e)–(g) converging orbits obtained for −0.65 V/SCE, (e) high $^3H_2O_2$ concentration; (h)–(j) core toroids with rolled orbits obtained for −0.75 V/SCE, (h) high $^3H_2O_2$ concentration.

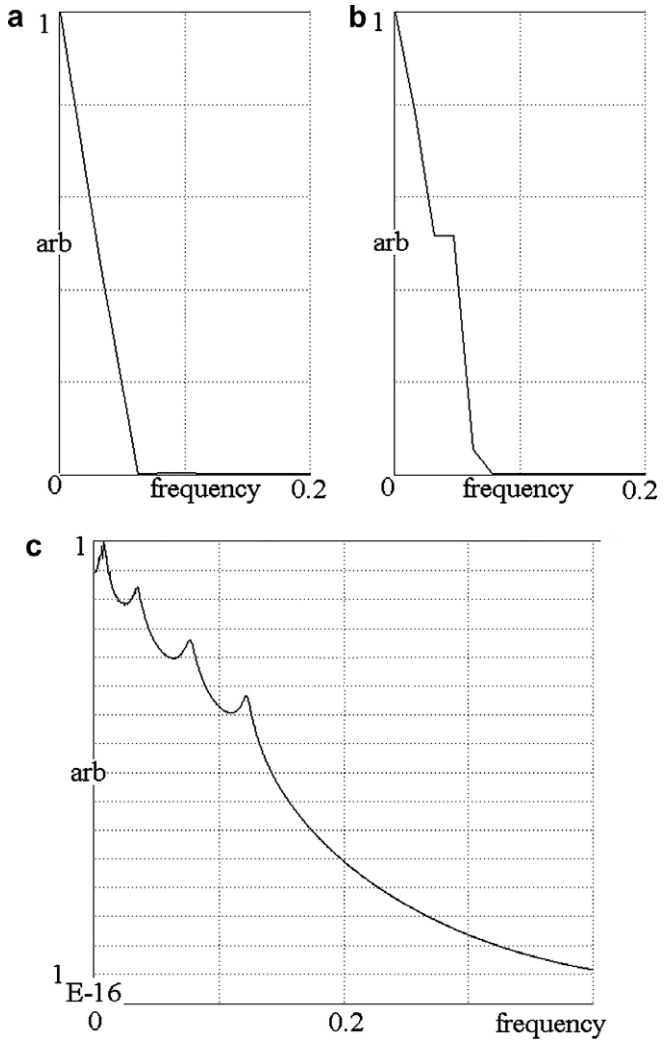

Fig. 12. Graphs of data of the power spectrum versus the frequency for potential instability analysis in Fig. 10. (a) Uniform distribution indicating chaos, (b) dominant peaks indicating a periodic system, and (c) broken line indicating a semi-periodic system.

and 1.27. The oscillations obtained for the Fig. 11(h–j) are thus classified as semi-chaotic and periodic owing to the positive and negative exponents [39]. This is confirmed in analyzing the power spectra of the noise records and the sinusoid which are characteristically quite different in giving a broken straight line or not broken or a few dominant peaks. Power spectra, describing the distribution of the power of a random process in the frequency domain, can be related to on the kinetic mode of unstable oxide layer formation when potential and hydrogen peroxide interact since the bond strength of Ti–O can be weak in regard to the stability of oxide. For the noise record corresponding to series in an uncorrelated stochastic signal (random and chaotic data), the power spectra is uniformly distributed over the frequency range (Fig. 12(a)) and is consistent with the phase space portrait. Whereas, the sinusoid record is in a stochastic process (periodic and quasi-periodic data) where the signal at any instant is dependent upon the immediately preceding event, the power spectra produces a few dominant peaks or a broken line (Fig. 12(b) and (c)). The loss of stochastic behavior with in a electrochemical noise record for unstable oxide processes would thus indicate the presence of deterministic behavior. For example, metastable oxide growth events associated with the passivity result in characteristic current transients and have subsequently been modeled. Fig. 7 shows the dynamic behavior of an under damped series electrical LC circuit. Analysis of the simulated time series in the line of the electrical circuit indicates a purely deterministic behavior, as indicated by the power spectra and the phase space portrait. Ti^{II} and Ti^{III} oxide is considered to nucleate randomly in time, with subsequent unstability in a deterministic mechanism. The analysis technique utilizing the chaotic test is therefore specifically designed to highlight the reduction in the stochastic behavior (e.g. any deterministic feature) in a time series, thereby revealing the presence of events such as Ti^{II} and Ti^{III} oxide growth. Ti^{II} and Ti^{III} oxide transients are more apparent for low hydrogen peroxide concentration, as indicated by the potential fluctuations, $\Delta\chi$ and the phase space portrait. This is characteristic of continued metastable oxide formation, and possibly indicates the development of generalized corrosion where the corrosion potential cannot be defined in the active region. Active corrosion event is active and, metastable oxide continues to take place. After the initial period of transients, a progressive termination event of the time signals is observed. The noise disappears to be associated with periodic then stable potential variations with the hydrogen peroxide concentration or potentials increasing indicating a stable activity. Finally, the dependency of phase space portrait and the power spectra on the semi-chaotic and semi-periodic fluctuations in potential with hydrogen peroxide means possible rearrangement and stability of oxide. Instabilities can also be analyzed from the dashed part in the equivalent circuit (Fig. 7). In this equivalent circuit, the dashed part can have several inductances and capacitances in parallel. Modeling with Mathematica™ program, values of capacitance and inductance are about $1–10^{-4}$ μF cm^{-2} and 10^{-4} H and frequency in this region is 5×10^5 Hz. Results are in the bifurcation diagrams in Fig. 13. Diagrams for instabilities (divergence) are in the graphs of

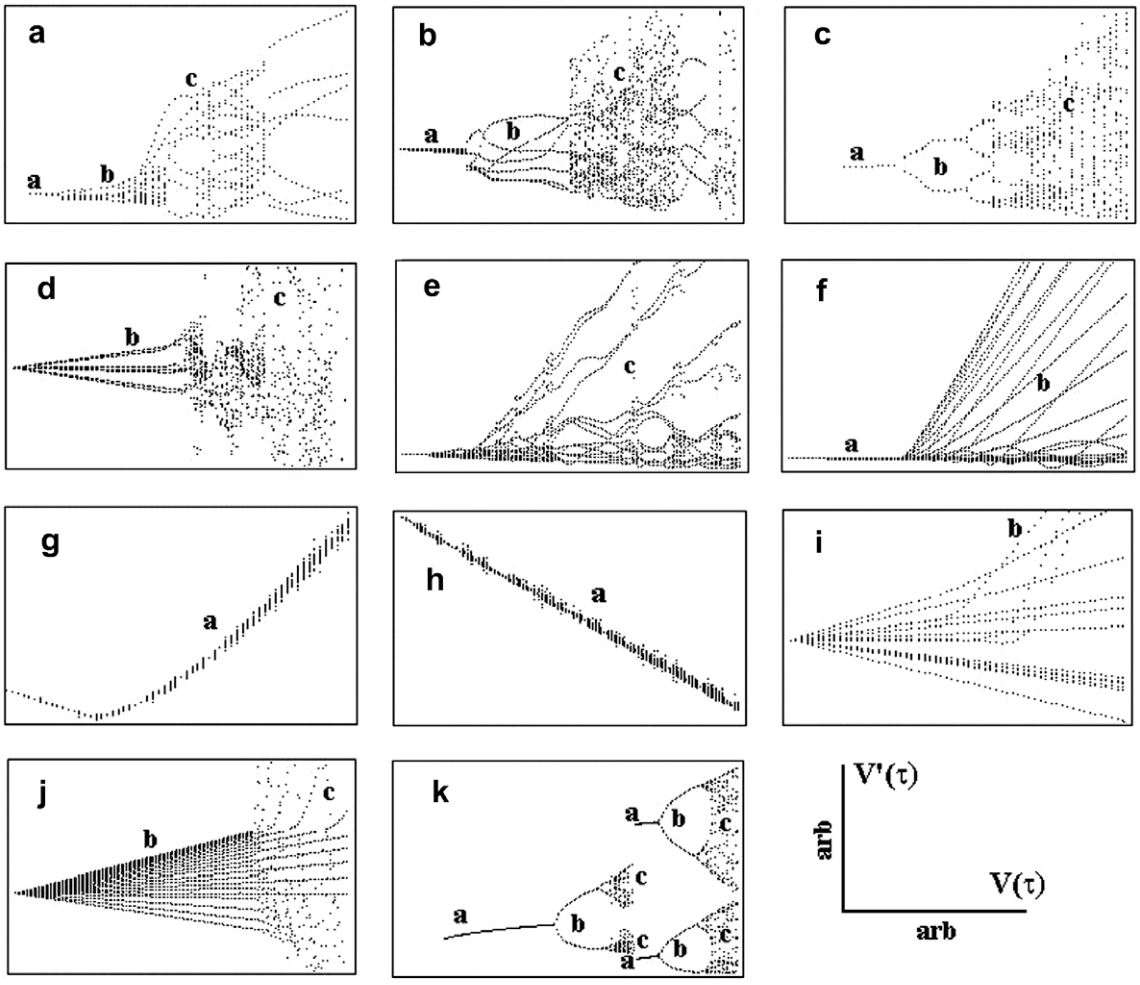

Fig. 13. Bifurcation diagrams. (a)–(e) chaos, (f)–(i) pseudo-stability and stability, (j)–(k) pseudo-stability (from Figs. 10 and 11), equivalent electrical circuit and Mathematica™.

(a)–(e), stability are in (f)–(i) and pseudo-stability in graphs of (j)–(k). In these diagrams, the region in (a) (convergence) shows how is large the stability potential, region in (b) with a fork bifurcation represents the pseudo-stability with several stationary states (metastable chaos). The region in (c) shows hysteresis with strange attractor common with the region in (b). Region in (c) is the chaotic state. The diagram in (a) shows a bifurcation cascade. In the diagram in (h), the plot corresponds to the stationary state, the diagram in (i) shows divergence, and in (k), the plot shows two subcritical bifurcations of Hapf leading to pseudo-stability. Thus, these methods are easy and invaluable tools for interpreting the stability of the oxide layer in low-energy radioactive water.

4. Conclusions

The simulated and the experimental analysis allowed monitoring the passivity of titanium in tritiated water containing radiolytic hydrogen peroxide at different concentrations. Electrochemical parameters indicate that the oxide (Ti^{IV}) formed in the tritiated water is limiting the charge transfer in the region of passivity under the influence of the high interfacial field after oxidation of transients (Ti^{II} and Ti^{III}) formed in the active region. This is in line with the increase of the hydrogen peroxide concentration, that can also be explained in terms of the formation of a more compact and insulating oxide. This oxide is formed of a hydroxylated outer layer and an inner layer with an insulating character. This insulating layer is responsible for the potential drop in the oxide. Once formed, the total thickness of oxide creates a strong electric field. In the case where the free potential is between the first and the second passivity, oxide is formed of two protective layers: a semiconductor and a dielectric layers leading to evidence that titanium is more protected. Consequently, when titanium is brought into contact with tritiated water, three phenomena will take place at the metal interface: (i) transients formation in active region where the corrosion potential is free at lower hydrogen peroxide concentration, (ii) passivity of the metal with formation of semiconductor TiO_2 at intermediate hydrogen peroxide concentration, and (iii) passivity with a dielectric layer formed by dehydration, coupled with a semiconductor layer at the upper passive potentials and high hydrogen peroxide concentration. In a perspective of application of titanium in the nuclear industry for a closed storage of tritiated water where the hydrogen peroxide and oxygen concentrations are large, the corrosion potential is easily in this passive region leading to evidence that protection with the semiconductor and dielectric layers is effective.

References

[1] A. Bruggeman, M. Snykers, P. de Regge, Fus. Technol. 14 (1988) 828.
[2] W.G. Burns, P.B. Moore, Radiat. Eff. 30 (1976) 233.
[3] J.K. Linacre, W.R. Marsh, Report R 10027, Chemistry Division, Atomic Energy Research Establishment, Harwell, 1981.
[4] J. Wright, J.K. Linacre, W.R. Marsh, T.H. Bates, in: Proceedings of the International Conference on the Peaceful Uses of Atomic Energy, vol. 7, United Nations, New York, 1956, p. 560.
[5] G. Bellanger, J.J. Rameau, J. Mater. Sci. 35 (2000) 1759.
[6] G. Bellanger, Corrosion Induced by Low-Energy Radionuclides – Modeling of Tritium and its Radiolytic and Decay Products Formed in Nuclear Installations, Elsevier, Amsterdam, 2004.
[7] P.E. Morris, R.C. Scarberry, Corrosion 26 (1970) 169.
[8] R.S. Schrebler Guzman, J.R. Vilche, A.J. Arvia, J. Appl. Electrochem. 11 (1981) 551.
[9] V. Cihal, Intergranular Corrosion of Steels and Alloys, SNTL, Prague, 1978, Elsevier, New York and Amsterdam, 1984.
[10] E. McCafferty, J.P. Wightman, T.F. Cromer, J. Electrochem. Soc. 146 (8) (1999) 2849.
[11] C. Law Jr., J. Newman, J. Electrochem. Soc. 126 (1979) 2150.
[12] P. Ponthiaux, F. Wenger, J. Galland, J. Electrochem. Soc. 142 (1995) 2204.
[13] Yu V. Pleskow, in: J.O'. M. Bockris, B.E. Conway, E. Yeager (Eds.), The Double Layer, vol. 1, Plenum, New York, 1981.
[14] J.P. Randin, in: J.O'.M. Bockris, B.E. Conway, E. Yeager (Eds.), Electrochemical Materials Science, vol. 4, Plenum, New York, 1984.
[15] D.D. MacDonald, B. Roberts, Electrochim. Acta 23 (1978) 781.
[16] A.J. Calandra, N.R. De Tacconi, R. Pereiro, A.J. Arvia, Electrochim. Acta 19 (1974) 901.
[17] J.M. McLaren, J.B. Pendry, P.J. Rous, D.K. Saldin, G.A. Somorjai, M.A. Van Hove, D.D. Yvedensky, Surface Crystallographic Information Service, A Handbook of Surface Structure, Reidel, Dordrecht, 1987.
[18] J.B. Pendry, Surface Crystallographic Information Service, Data Base and Graphics Programs, Riedel, Dordrecht, 1987.
[19] Kazuhisa Azumi, Masahiro Seo, Corros. Sci. 43 (2001) 533.
[20] J.R. MacDonald, Impedance Spectroscopy, John Wiley, New York, 1987.
[21] J.B. Bessone, D.R. Salinas, C.E. Mayer, M. Ebert, W.J. Lorenz, Electrochim. Acta 37 (12) (1992) 2283.
[22] T. Shibata, Y.-C. Zhu, Corros. Sci. 37 (2) (1995) 253.
[23] C. Fonseca, M.A. Barbosa, Corros. Sci. 43 (2001) 547.
[24] C.Y. Chao, L.F. Lin, D.D. MacDonald, J. Electrochem. Soc. 129 (1982) 1874.
[25] P. Schmuki, H. Böhni, Electrochim. Acta 40 (1995) 775.
[26] A. Le Mehaute, J. Stat. Phys. 36 (1984) 665.
[27] G. Boschloo, D. Fitzmaurice, J. Electrochem. Soc. 147 (2000) 1117.
[28] K. Ueno, S.-I. Pyun, M. Seo, J. Electrochem. Soc. 147 (12) (2000) 4519.
[29] N. Wüthrich, Electrochim. Acta 25 (1980) 819.
[30] N. Wüthrich, Electrochim. Acta 26 (1981) 1617.
[31] D.A. Vermilyea, J. Electrochem. Soc. 110 (1963) 345.
[32] M.A. Butler, D.S. Ginley, J. Electrochem. Soc. 135 (1988) 45.
[33] J.A. Wharton, B.G. Mellor, R.J.K. Wood, C.J.E. Smith, J. Electrochem. Soc. 147 (9) (2000) 3294.
[34] G. Bellanger, Corros. Sci. 48 (2006) 1379.
[35] G. Bourceanu, V. Melnig, J. Vatamanu, R. Vasiliu, Electrochim. Acta 43 (9) (1998) 1031.
[36] Tim G.J. van Venrooij, M.T.M. Kopper, Electrochim. Acta 40 (11) (1995) 1689.
[37] D. Sazou, M. Pagitsas, Electrochim. Acta 38 (6) (1993) 835.
[38] H. Mayet, B. Baroux, in: Electrochemical Society Proceedings, vol. 15, Electrochemical Society, Inc., Pennington, USA 95, 1995, p. 358.
[39] S.G. Corcoran, K. Sieradzki, J. Electrochem. Soc. 139 (1986) 2459.